

Vision-based kinematic calibration of a H4 parallel mechanism : Practical accuracies

Nicolas Andreff^{1,2} Pierre Renaud³ Philippe Martinet²
François Pierrot³

¹ LaRAMA, U. Blaise Pascal/IFMA, Clermont-Ferrand, France,
`Nicolas.Andreff@ifma.fr`

² LASMEA, U. Blaise Pascal/CNRS, Clermont-Ferrand, France,
`martinet@lasmea.univ-bpclermont.fr`

³ LIRMM, U. Montpellier II/CNRS, Montpellier, France,
`renaud|pierrot@lirmm.fr`

Abstract

In this article, we present the kinematic calibration of a H4 parallel robot using a vision-based measuring device. Calibration is performed according to the inverse kinematic model method, using first the design model then a model developed for calibration purpose. To do so, the end-effector pose has to be measured with the utterst accuracy. Thus, we first evaluate the practical accuracy of our vision-based measuring system to have a precision in the order of magnitude of $10\mu m$ and $10^{-3}deg$. Second, we calibrate the robot using our vision system, yielding a final positioning accuracy of the end-effector lower than 0.5mm.

1 Introduction

Compared to serial mechanisms, parallel structures may exhibit a much better repeatability [Mer97], but their large number of links and passive joints often limits their performance in terms of accuracy [WM93]. A kinematic calibration is thus needed. The algorithms proposed to conduct calibration for parallel structures can be classified in three classes: methods based on the direct use of a kinematic model, on the use of kinematic constraints on mechanism parts, and methods relying on the use of redundant proprioceptive sensors.

The use of additional proprioceptive sensors on the passive joints of the mechanism enables one to have a unique solution to the direct kinematic model [TTM95], and to perform the kinematic calibration [WA92, Zhu97, Dan00], or to improve their accuracy [MCKP02]. Practically speaking, the

mechanism design has to take into account the use of such extra sensors. Nevertheless, not all kinds of mechanisms can be equipped with additional sensors.

Methods based on kinematic constraints of the end-effector [Dan00] or the legs [GH94a, ZR93, KB99, Dan99] solve this problem. However, the former methods are not numerically efficient [Dan00], and kinematic constraints of the legs of the mechanism in position or orientation seem difficult to achieve in practice on large structures.

The forward kinematic model of parallel structures can rarely be expressed analytically [Mer97]. The use of this model to achieve kinematic calibration may consequently lead to numerical instability [Dan00]. On the other hand, the inverse kinematic model can usually easily be derived. Calibration can then be performed by comparing the measured joint variables and their corresponding values estimated from the measured end-effector pose and the inverse kinematic model. Each leg can furthermore be calibrated independently [ZYM98]. Up to now, the inverse kinematic model method seems the most efficient method [Dan00].

Its main limitation is the need for accurate measurement of the full end-effector pose (*i.e.* both its position and its orientation). Among the proposed measuring devices [CSP99, VPG94, MJ95, SZ99], only a few have been used to conduct kinematic identification of a parallel structure [ZYM98, GH94b, FDAF96, VC98]. Indeed, the systems are either very expensive, tedious to use or with low working volume. On the opposite, a vision-based measuring system enables one to perform the pose measurement accurately [RADM02], is low-cost and easy to use. Using this device and the inverse kinematic method may therefore be an efficient way to conduct kinematic calibration.

In this article, we present the vision-based kinematic calibration of a H4 robot [PMCG01], focusing on experimental accuracies of the calibration process as well as of the vision system itself (see [Ren03] for details). In section 2, two different kinematic models are detailed. The first one (Model 12) corresponds to the initial design of the mechanism, and the second one (Model 31) is developed for calibration purpose. Then, section 3 addresses briefly the specific problems due to the use of a vision-based measuring system for kinematic calibration. The identifiability conditions bound to the use of such an exteroceptive sensor are underlined. Section 4 is devoted to the presentation of the methodology used for evaluating the practical accuracy of our vision-based measuring device. Experimental results, given in Section 5, split in two parts : first, we evaluate a precision in the order of $10\mu m$ and 10^{-3} deg for the end-effector pose measurement; second, using our vision system, we calibrate a H4 prototype, performing statistically independent validation experiments and showing a final positioning accuracy of the end-effector of less than $0.5mm$. The calibration gain induced by the use of the calibration model is discussed. Finally conclusions are given on the use of a vision-based measuring device for the calibration of this class

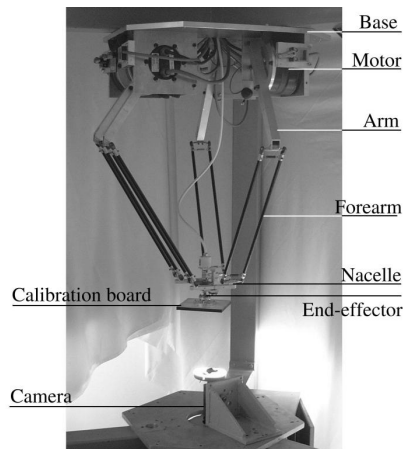


Figure 1: H4 and vision-based measuring system

of mechanisms.

2 Kinematic Modeling

2.1 H4 Description

The H4 mechanism (Fig. 1) is a parallel mechanism composed of four chains, actuated by four angular motors located between the base and the arms. The forearms linking the arms and the nacelle are composed of two rods. The end-effector has four degrees of freedom (three translations and one rotation) if the closed loops constituted by these four pairs of rods correspond to spatial parallelograms [PMCG01]. The end-effector is linked to the nacelle with a mechanical amplification system to achieve a higher rotation capability.

2.2 Model 12

2.2.1 Hypotheses

In the following, the end-effector will be assumed to have only four degrees of freedom. The hypothesis validity will be discussed in paragraph IV. Since each forearm parallelogram is assumed perfect, it is thus equivalent to a link ensuring a circular translation of the nacelle with respect to the arm. In this part, we assume furthermore that the rotary joint centers $P_i, i \in [1, 4]$ between the base and the arms are located in the same plane, at equal distance R from the corresponding joint centers A_i on the nacelle when this latter is considered to be in the base plane (Fig. 2). The four arms are supposed to be of equal length L , and the forearms of length l . Considering

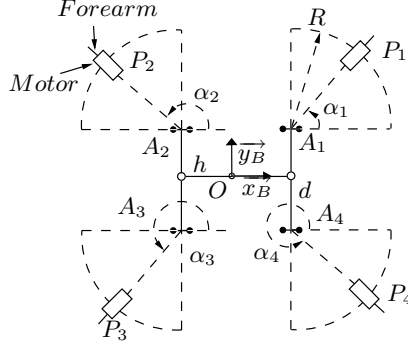


Figure 2: Location of the joints between base and forearms

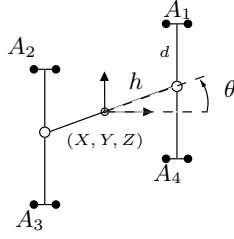


Figure 3: Definition of the nacelle's angle

the nacelle dimensions h and d (Fig. 3), the mechanism geometry is therefore defined by nine parameters : R, l, L, h, d, α_i with $i \in [1, 4]$. With such a model, parameter d has however no influence on the kinematics [PMCG01]. Taking into account the joint offsets q_{i0} , $i \in [1, 4]$, twelve parameters finally define the mechanism kinematics.

2.2.2 Inverse Kinematic Model

An implicit model can be readily written between the end-effector pose (X, Y, Z, θ) (Fig. 3) and the joint variables by expressing the i -th forearm length, $i \in [1, 4]$ as a function of the parameters [PMCG01]:

$$L^2 - l^2 - \|\overrightarrow{P_i A_i}\|^2 = -2 \begin{pmatrix} \overrightarrow{P_i A_{ix}} \cdot l \cdot \cos(\alpha_i) \cdot \cos(q_i) \\ + \overrightarrow{P_i A_{iy}} \cdot l \cdot \sin(\alpha_i) \cdot \cos(q_i) \\ - \overrightarrow{P_i A_{iz}} \cdot l \cdot \sin(q_i) \end{pmatrix} \quad (1)$$

The inverse kinematic model can then be derived from this implicit model [PMCG01]:

$$q_i = 2 \cdot \text{Atan} \left(\frac{N + \epsilon_i \sqrt{N^2 + M^2 - G^2}}{G + M} \right), i \in [1, 4] \quad (2)$$

with

$$G = L^2 - l^2 - \|\overrightarrow{P_i A_i}\|^2, N = 2 \cdot l \cdot \overrightarrow{P_i A_{iz}}$$

Table 1: Model 31 kinematic parameters

Designation	Parameter
$x_i, y_i, z_i, i \in [2, 4]$	Rotary joint positions
$\psi_i, \beta_i, i \in [1, 4]$	Rotary joint orientations
$q_{i_0}, i \in [1, 4]$	Joint offsets
$l_i, L_i, i \in [1, 4]$	Arm and forearm lengths
h, d	Nacelle dimensions

$$M = -2.l.(\overrightarrow{P_i A_{ix}}.cos(\alpha_i) + \overrightarrow{P_i A_{iy}}.sin(\alpha_i))$$

and $\epsilon_i = \pm 1$ depending on the assembly.

2.2.3 Calibration method

To identify the parameter vector ξ , an error function is minimized, which compares the estimated joint variables and the measured ones \tilde{q} for N different end-effector poses $(X_j, Y_j, Z_j, \theta_j)$:

$$\min_{\xi} \sum_{j=1}^N \sum_{i=1}^4 (q_i(\xi, X_j, Y_j, Z_j, \theta_j) - \tilde{q}_{ij})^2 \quad (3)$$

2.3 Model 31

2.3.1 Hypotheses

The former geometry corresponds to the mechanism design. Due to the manufacturing tolerances, assembly errors, the previous assumptions about the geometry may be questionable. In this part, the mechanism is still considered as a four degrees of freedom mechanism and the nacelle is assumed to be planar with dimensions h et d . On the other hand, no assumption is now made about the position and orientation of the revolute joints between the base and the arms, nor on the arm and forearm lengths.

The base frame is attached to the first joint center P_1 (Fig. 4), its axis $\overrightarrow{z_B}$ parallel to the end-effector rotation axis, and orientation defined by the ‘‘H-configuration’’ of the nacelle. The position of the joint centers P_i is defined relatively to the corresponding joint centers on the nacelle in a similar way to the Model 12. The joint axis $\overrightarrow{z_i}$ are defined by Euler angles ψ_i and β_i . Thirty-one parameters are then necessary to define its geometry (Table 1).

2.3.2 Implicit model

The implicit model can be obtained as in 2.2 for each kinematic chain $i \in [1, 4]$:

$$\|L_i \overrightarrow{V_i} + \overrightarrow{W_i}\|^2 = l_i^2 \quad (4)$$

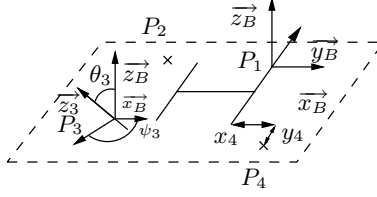


Figure 4: Definition of the base frame and orientation of rotary joint between base and arm for the Model 31

with

$$\vec{V}_i = \begin{pmatrix} \sin(q_i+q_{i0})\cos(\beta_i)\sin(\psi_i)-\cos(q_i+q_{i0})\cos(\psi_i) \\ -\sin(q_i+q_{i0})\cos(\beta_i)\cos(\psi_i)-\cos(q_i+q_{i0})\sin(\psi_i) \\ -\sin(q_i+q_{i0})\sin(\beta_i) \end{pmatrix}$$

$$\vec{W}_i = \begin{pmatrix} X-x_i+(1+\epsilon_{1i}-\epsilon_{2i}\cos(\theta))h \\ Y-y_i+d-\epsilon_{2i}h\sin(\theta) \\ Z-z_i \end{pmatrix}$$

and $\epsilon_{1i} = \pm 1$, $\epsilon_{2i} = \pm 1$ depending on the assembly. The inverse kinematic model consists in expressing q_i as a function of (X, Y, Z, θ) , which is analytically tedious.

2.3.3 Calibration method

The parameter vector ξ is obtained from the implicit model by solving:

$$\min_{\xi} \sum_{j=1}^N \sum_{i=1}^4 \left(l_i - \|L_i \vec{V}_{ij} + \vec{W}_{ij}\| \right)^2 \quad (5)$$

3 From Vision to Calibration

In this part, we consider how to use vision to perform the kinematic calibration of the H4 mechanism.

3.1 Vision-based measurement characteristics

The vision-based measuring system is composed of a camera, fixed onto the base, and a calibration board fixed onto the end-effector (Fig. 1). The system is calibrated at the beginning of the experiment by acquiring a sequence of about 8 images, using a software developed at LASMEA [LVD98]. After calibration, the pose ${}^C T_{cb}$ of the calibration board with respect to the camera can be computed for each image [DRLR89]. Furthermore, the measuring system is easy to use, and the experimental procedure for the kinematic calibration is fast.

3.1.1 From Image to Pose

The camera being calibrated, the image is supposed to respect the pin-hole model [HM93]. Recall that the image coordinates (x, y) of a point are related to its coordinates (X, Y, Z) in the calibration board frame by the perspective projection:

$$s \begin{pmatrix} x \\ y \\ 1 \end{pmatrix} = \begin{pmatrix} KR & Kt \end{pmatrix} \begin{pmatrix} X \\ Y \\ Z \\ 1 \end{pmatrix} \quad (6)$$

with ${}^C T_{cb} = (R, t)$ the pose to determine, K the intrinsic parameters of the camera. This projection equation is only defined to an arbitrary factor s . The intrinsic parameters related to this model, including optical distortions, are determined during the calibration of the measuring system. In practice, the pose ${}^C T_{cb}$ is determined by non-linear optimization [DRLR89].

3.1.2 Using the pose

The full-pose measurement enables one to perform calibration using either the inverse kinematic model (3) or the implicit kinematic model (5). In this method, the end-effector pose ${}^B T_{ee}$ is defined by its position and orientation with respect to the base frame, and related to the pose measurement by the relation:

$${}^B T_{ee} = {}^B T_C {}^C T_{cb} {}^{cb} T_{ee} \quad (7)$$

Two transformations have therefore to be identified simultaneously with the kinematic parameters: ${}^B T_C$ between the camera and base frames, and ${}^{cb} T_{ee}$ between the calibration board and the end-effector.

3.2 Prior Kinematic Analysis

Information about the kinematics of the system can be obtained before conducting the identification process. Indeed, the H4 robot has a constant rotation axis, perpendicular to the nacelle, provided that the assumption concerning the forearm parallelograms is valid. Consequently, the calibration board also rotates around this constant axis. The latter can hence be immediately estimated in the camera frame since the rotation matrix between the calibration board and the camera ${}^C R_{cb}$ can be computed for each end-effector pose. Furthermore, as the rotation axis corresponds to the vector \vec{z}_b , this vector can be identified in the camera frame R_C . This enables us to reduce the number of kinematic parameters identified simultaneously.

3.3 Identifiability

3.3.1 Model 12

Identifying ${}^C T_B$ and ${}^{cb} T_{ee}$ is equivalent to base-world and tool-hand calibration problems. Since the calibration board movement is limited to one rotation w.r.t the camera, the transformation ${}^{cb} T_{ee}$ cannot be completely identified [TL89, AHE01]. Moreover, in our context, due to visibility condition of the calibration board, the camera and calibration board are approximately aligned with the mechanism rotation axis (Fig. 1). Then expanding (7) shows that $z_{cb,ee}$ and $z_{B,C}$ (the translation components along z of the transformations ${}^{cb} T_{ee}$ and ${}^C T_B$) can be identified only by their sum. Finally, as the angles defining parallelism between the end-effector and the calibration board have only a second-order influence, their identification seems also tedious. Hence the *a priori* value of these parameters will then be used. These remarks have been confirmed by the numerical estimation of the Jacobian matrix.

3.3.2 Model 31

This model is also invariant with respect to a simultaneous rotation of the location of the joints between the base and the legs, the camera frame and the calibration board frame around the axis \vec{z}_B . Therefore, one parameter between the two corresponding angles of the transformations ${}^B T_C$ and ${}^{cb} T_{ee}$ has here again to be fixed to its *a priori* value. In the same way, the nacelle dimension d and the translation component $y_{B,C}$ of the transformation ${}^B T_C$ are only identifiable by their sum. The *a priori* value of the parameter d is then used.

The identification by the inverse kinematic model method is therefore submitted to two identifiability problems: The first one is the number of degrees of freedom of the mechanism, that prevents from achieving the complete calibration of the transformations related to the measuring device. The second one comes from the number of degrees of freedom introduced in the joint location parameterization for the Model 31. We can also remark that the identification of the transformations related to the measuring device imply a global identification of the mechanism, and not the independent identification of each kinematic chain.

4 Measuring System Evaluation

The measuring system evaluation is achieved by conducting simultaneous measurements with the vision-based system and a laser interferometer on a high-speed machine-tool axis (Figures 5 and 6). It consists in estimating trueness, expressed in terms of bias, and precision. Trueness is the closeness of agreement between the average value obtained from a large series of test

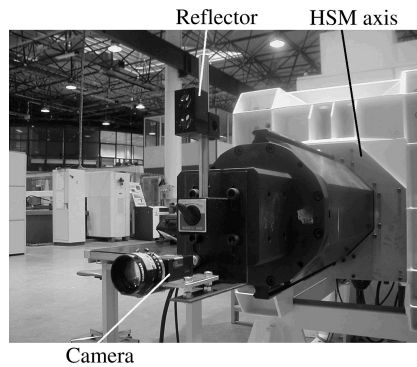


Figure 5: Camera and reflector on a high-speed machine-tool axis.

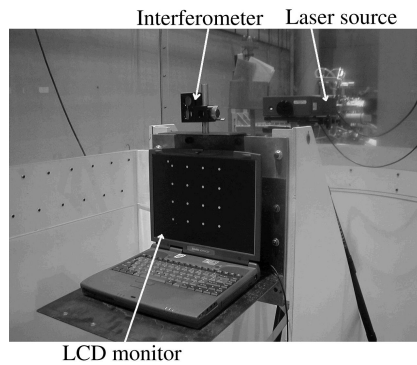


Figure 6: Interferometer, LCD monitor and laser source.

results and an accepted reference value and precision the closeness of agreement between independent test results obtained under stipulated conditions [ISO94].

4.1 Laser Interferometer Measurement Principle

The laser interferometer set-up consists of a laser source and 2 optics : an interferometer (Figure 6) and a reflector (Figure 5). A single degree of freedom is measured for each laser interferometer configuration, defined by the mounted optics. Only a differential measure is provided: an initial pose has to be arbitrarily defined in order to express the measured displacement. Nevertheless, optics have to be modified to access to the different degrees of freedom. Measurements are therefore not expressed in a common coordinate frame.

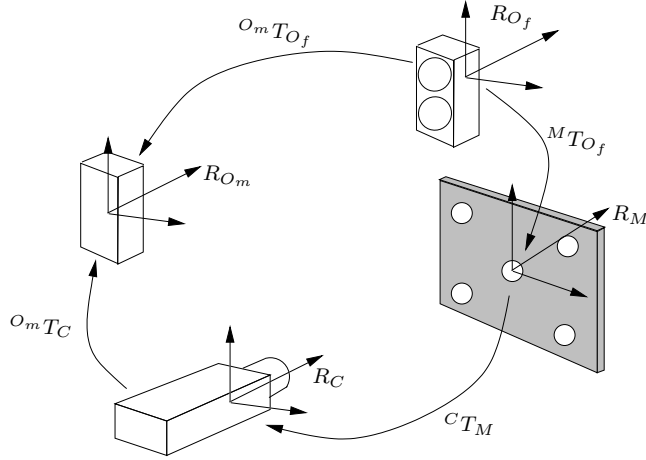


Figure 7: Measurement coordinate frames and associated transformations.

4.2 Measurement Coordinate Frames

The laser interferometer measures some of the components of $O_m T_{O_f}$, the transformation from R_{O_m} , the reflector coordinate frame, to R_{O_f} , the interferometer coordinate frame (figure 7). The vision-based system measures $C T_M$, the transformation from the camera coordinate frame R_C to the calibration board frame R_M . During each experimentation, the calibration board and the interferometer are rigidly linked and their relative position can be defined by $M T_{O_f}$, transformation between their respective coordinate frames. In the same way, the reflector and the camera are rigidly linked and their relative position defined by the transformation $O_m T_C$. Notice that interferometric and vision-based measurements are not expressed in the same coordinate frames.

4.3 Precision Estimation

The evaluation of the measuring system consists in determining measurement trueness and precision. Pose measurements, achieved for different axis positions, include the axis behavior and measurement errors. Consecutive positions are chosen close enough so that the pose difference can be considered only due to the measurement error. The measurement standard deviation is then computed from the set of pose differences in the calibration board coordinate frame.

4.4 Trueness Estimation

The trueness estimation is achieved considering interferometric measures to be reference values. For comparison sake only, vision-based measures have to

be expressed in the interferometer coordinate frame. For each axis position i , the transformation between the interferometer and reflector frames can be expressed as a function of the vision-based measurement:

$${}^{Om}T_{Of}^i = {}^{Om}T_C {}^C T_M^i {}^M T_{Of} \quad (8)$$

As interferometric measures are differential, equation (8) is expressed between two consecutive measurement positions i and $i + 1$:

$${}^{Om}T_{Of}^i ({}^{Om}T_{Of}^{i+1})^{-1} = {}^{Om}T_C {}^C T_M^i ({}^C T_M^{i+1})^{-1} ({}^{Om}T_C)^{-1} \quad (9)$$

The measurement coordinate frames are positioned such that frame orientations are almost identical. The angles characterizing the previously defined transformations remain therefore to a small amplitude, and (9) can be linearized:

$$\left\{ \begin{array}{l} \Delta\alpha_{OmOf} = \Delta\alpha_{CM} \\ \Delta\beta_{OmOf} = \Delta\beta_{CM} \\ \Delta\gamma_{OmOf} = \Delta\gamma_{CM} \\ \Delta x_{OmOf} = -\Delta\gamma_{CM} \cdot y_{MOf} + \Delta\beta_{CM} \cdot z_{MOf} \\ \quad + \Delta x_{CM} - \gamma_{OmC} \cdot \Delta y_{CM} + \beta_{OmC} \cdot \Delta z_{CM} \\ \Delta y_{OmOf} = \Delta\gamma_{CM} \cdot x_{MOf} - \Delta\alpha_{CM} \cdot z_{MOf} \\ \quad + \gamma_{OmC} \cdot \Delta x_{CM} + \Delta y_{CM} - \alpha_{OmC} \cdot \Delta z_{CM} \\ \Delta z_{OmOf} = -\Delta\beta_{CM} \cdot x_{MOf} + \Delta\alpha_{CM} \cdot y_{MOf} \\ \quad - \beta_{OmC} \cdot \Delta x_{CM} + \alpha_{OmC} \cdot \Delta y_{CM} + \Delta z_{CM} \end{array} \right. \quad (10)$$

Thus, the angular variations are directly comparable. However, 6 parameters related to the experimental set-up ($x_{MOf}, y_{MOf}, z_{MOf}, \alpha_{OmC}, \beta_{OmC}, \gamma_{OmC}$) have to be estimated in order to compare the translation displacement measures. As these parameters interfere linearly in (10), a least-squares estimation can be computed. Estimation bias is reduced by performing parallel filtering of the linear system [Ric98].

Due to the use of the laser interferometer, measurement path has to be linear. This exciting trajectory [KD99] is too weak to allow the identification of the 6 parameters. For each interferometer measurement configuration, only two parameters can be identified, and the other parameter *a priori* values are employed. Bias analysis is consequently rather delicate.

5 Experimentation

5.1 Vision-based measurement accuracy

5.1.1 Set-up

The measuring system is composed of a CCD camera (Figure 5), fixed on the moving part, and a calibration board, composed of several dots. The calibration board is generated using a LCD monitor (Figure 6).

The high-speed machine-tool axis stroke is equal to $400mm$. A Renishaw ML10 interferometer is employed, with a fixed interferometer (Figure 6) and a moving reflector (Figure 5). Three measuring system set-ups were experimented in order to evaluate the influence of the calibration board size, focal length and sensor resolution. In the first case, the camera has a resolution of 768×576 pixels, 8bit-encoded with a $50mm$ lens. For the second set-up, the same camera is equipped with an $8mm$ lens. For the third set-up, the camera has a resolution of 1024×768 pixels, 8bit-encoded with a $6mm$ lens. Images are stored on a PC via a video capture board. Calibration boards are displayed on a $14''$ LCD screen, with a 1024×768 pixels resolution.

The axis displacement between two measurements is equal to $5mm$. For each position, 10 images are stored and their average value is considered for the pose evaluation, in order to reduce high-frequency noise. The axis displacement direction z corresponds roughly to the camera axis.

5.1.2 Screen-displayed Calibration Boards

Measurement accuracy is bound to the quality of determination of the dot centers and to the sensitivity of the optimisation process to the components of the pose ${}^C T_{cb}$.

The determination of the dot centers is achieved by identifying gray-level variations in the image with the contour of the dots. By using calibration boards generated with the LCD monitor, the geometry of the dots and the gray-level variations can be precisely defined in order to ensure a more accurate localization of the dot centers than with physical calibration blocks.

Pose estimation accuracy increases with the size of the calibration board image. However, the calibration board has to stay in the field of view of the camera for any measurement configuration. In order to meet these two requirements, several calibration boards, with different sizes, are generated on the LCD monitor. For each camera position, the largest visible calibration board i is used to determine the pose ${}^C T_{cb_i}$, which defines the transformation from the calibration board coordinate frame R_{Mi} to the camera coordinate frame R_C . The set of calibration boards is generated with a common coordinate frame, which enables one to express finally all the pose measurements in a single coordinate frame. The ratio measurement volume/accuracy can therefore be increased by the use of screen-displayed calibration boards.

5.1.3 Precision

First measurement set-up With a $50mm$ lens, the calibration board image size is almost constant during the axis displacement. First measurements were then achieved using a single calibration board, to minimize influence of image size. The measuring system precision is higher for displacement measurements along x and y axis and rotation around the z axis (Table 2 - Set-up

Table 2: Estimated standard-deviations.

D.o.f	Set-up 1	Set-up 2	Set-up 3
R_x	0.105°	$1.8E - 3^\circ$	$1.5E - 3^\circ$
R_y	0.110°	$1.5E - 3^\circ$	$1.6E - 3^\circ$
R_z	$1.4E - 3^\circ$	$1.8E - 3^\circ$	$1.0E - 3^\circ$
T_x	$3.17\mu m$	$3.98\mu m$	$2.6\mu m$
T_y	$3.98\mu m$	$4.53\mu m$	$3.0\mu m$
T_z	$135\mu m$	$18\mu m$	$12\mu m$

1). This behavior is bound to the measuring principle and the measurement configuration: displacements in the calibration board plane are directly perceptible in the camera image, contrary to displacements orthogonal to the board plane.

Influence of the Calibration Board Size A second calibration board, observable for $0 < z < 200mm$, is computed to quantify the influence of the calibration board size. A significant decrease of the estimated standard deviations is observed: precision is increased by about 45% for a size modification of 60%. Hence, the interest of multiple screen-displayed calibration boards is confirmed.

Influence of the Focal Length For the second set-up, the image size variation is higher, with a smaller calibration board image for $z = 0$. The measuring precision is however significantly higher (Table 2 - Set-up 2). This precision increase is certainly due to the better respect of the pin-hole model.

Influence of the CCD Resolution With the third set-up, precision is increased by approximately 30% (Table 2 - Set-up 3). This increase can be attributed to the combination of a shorter focal length and a higher CCD resolution.

In terms of precision, the displacement measurements in the calibration board plane directions are comparable to the interferometric ones (Table 3). For this instrument, rotation around z cannot be measured. The vision-based measuring system also provides us simultaneously with accurate measurement of rotations.

5.1.4 Trueness

First Measurement Configuration An angular measurement bias can be observed on figures 8, 9. Translation measurement bias in x and y directions remain of small amplitude (figures 10, 11, 12), with an order of

Table 3: Interferometer specifications.

D.o.f	Interferometer specification
R_x	$1.7E - 5^\circ$
R_y	$1.7E - 5^\circ$
R_z	<i>non - measurable</i>
T_x	$1.15\mu m$
T_y	$1.15\mu m$
T_z	$0.35\mu m$

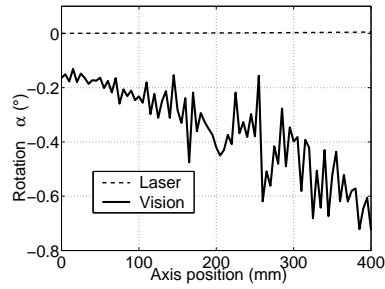


Figure 8: Rotation around x w.r.t position $z = 0$.

$0.01mm$. Their quantification is however quite delicate because of the previously underlined identification problem.

Influence of Calibration Board Size Increasing pose estimation sensitivity to rotations, by modifying calibration board size, lowers significantly measurement bias. For the axis positions where the second calibration board can be observed, measurement bias is reduced by a factor 3.

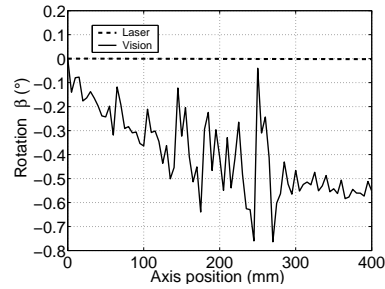


Figure 9: Rotation around y w.r.t position $z = 0$.

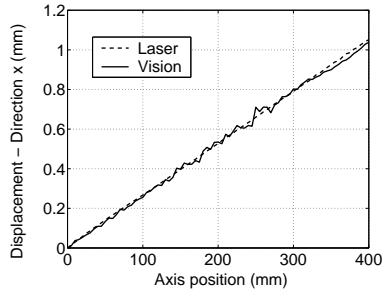


Figure 10: Translation along the x axis in the interferometer coordinate frame - Reference $z = 0$.

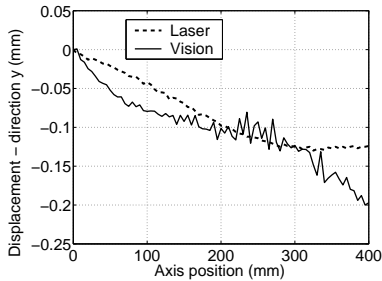


Figure 11: Translation along the y axis in the interferometer coordinate frame - Reference $z = 0$.

Influence of the Focal Length and CCD Resolution The measurements with set-ups 2 and 3 have been achieved without the interferometer. The bias estimation procedure cannot therefore be applied. However, since the axis repeatability is very high, presence of bias can be evaluated by the amplitude of the measured angular variations. In the second measurement set-up, the use of a 8mm lens leads to angular variations comparable to the variations previously measured with the interferometer. Trueness seems therefore sharply increased with the use of this lens. Modification of the sensor resolution (Set-up 3) does not modify significantly the measurement bias.

5.2 Calibration of the H4

5.2.1 Set-up

The camera sensor has a resolution of 1024×768 pixels, 8bit encoded, with a 3.8 mm lens. Images are stored on a PC via an IEEE1394 bus. For each position, 10 images are stored and their average value is considered for the pose evaluation, in order to reduce high frequency noise. The pose can

be measured with accuracy in the order of respectively 0.2 mm and 0.03° for each translation and rotation component. This lower accuracy comes from the fact that we could not use the LCD monitor. Indeed, during the calibration process, the LCD monitor is observed by the camera under too sharp angles of view to get enough contrast in the image. Therefore, we had to use a standard calibration board made of retroreflective dots.

Eighty-one poses are used, equally distributed in a $200 \times 200 \times 150 \text{ mm}^3$ volume, with three different orientations ($\theta = -20^\circ, 0^\circ, 20^\circ$). Out of them, seventy-one poses are randomly chosen for the calibration, the other ten are used to perform a validation test.

5.2.2 Kinematic Analysis

The variation of the rotation axis in the camera frame is quantified by the variation of the angle between the axis and its mean direction. The estimated standard deviation is equal to 0.12° . The amplitude of the axis direction variation confirms that the mechanism can be safely considered as having four degrees of freedom.

5.2.3 Identification

Model 12 The computation of the estimated parameters is achieved using the inverse kinematic model method, with non-linear optimization. The Levenberg-Marquardt algorithm is used, and columns of the identification Jacobian matrix are scaled with extremal scaling value [Sch93] to avoid biased estimation. The identified parameters related to the mechanism are listed in Table 4, and compared to their *a priori* values.

It is noticeable that using the *a priori* parameters, rather than the optimally estimated ones, yields an average positioning error of the nacelle of 26 mm and 0.022 rad .

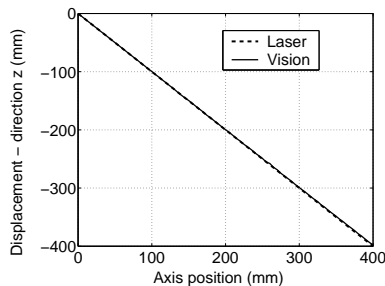


Figure 12: Translation along the z axis in the interferometer coordinate frame - Reference $z = 0$.

Table 4: *A priori* and identified kinematic parameters of the model 12 (IS units)

	h	l	R	L
<i>a priori</i>	0.060	0.2600	0.1400	0.4800
Identified	0.0610	0.2600	0.1413	0.4876
	α_1	α_2	α_3	α_4
<i>a priori</i>	0	3.1416	4.7124	4.7124
Identified	-0.0015	3.1016	4.6807	4.6859
	q_{01}	q_{02}	q_{03}	q_{04}
<i>a priori</i>	0	0	0	0
Identified	-0.0662	-0.0080	-0.0476	-0.0561

Table 5: Mean and root mean square errors on joint variables (*rad*)

Variable	q_1	q_2	q_3	q_4
Before calibration				
Mean	9.0^{E-2}	3.5^{E-2}	7.3^{E-2}	8.3^{E-2}
R.M.S	9.0^{E-2}	3.7^{E-2}	7.4^{E-2}	8.3^{E-2}
After calibration - Model 12				
Mean	7.1^{E-5}	1.1^{E-4}	-7.7^{E-4}	-2.1^{E-4}
R.M.S	1.4^{E-3}	1.3^{E-3}	1.4^{E-3}	2.6^{E-3}
After calibration - Model 31				
Mean	-2.0^{E-4}	5.2^{E-4}	-4.7^{E-4}	7.4^{E-5}
R.M.S	2.9^{E-3}	2.6^{E-3}	1.8^{E-3}	3.1^{E-3}

Model 31 The angle around \vec{z}_B between the nacelle and the calibration board identified with the Model 12 is used to achieve the kinematic calibration with the second model. The *a priori* value of d is employed.

5.2.4 Validation

Joint residuals For Model 12, a first validation consists in estimating with the identified inverse kinematic model the joint variables from the ten pose measurements that were not used for calibration, and compare these values to the recorded joint variables. The mean and root mean square errors of the four joints are indicated in Table 5, showing an accuracy increase from some $0.1rad$ before calibration to some $10^{-4}rad$ afterwards. For Model 31, the validation is achieved by computing the errors committed in the joint variables estimation, to enable comparison with Model 12. The errors are of the same order.



Figure 13: Validation experiment - Kinematic constraint on the end-effector

Table 6: Straightness evaluation for the two experiments with initial and calibrated kinematic parameters

Direction	1	2
Before calib.	1.3^{E-3}	2.3^{E-3}
Model 12	4.9^{E-4}	5.8^{E-4}
Calib. model	5.9^{E-4}	1.1^{E-3}

Straightness evaluation To confirm these results independently from the measuring device, an experiment is conducted where the end-effector is manually constrained to follow a line materialized by a ruler (Fig. 13). The corresponding joint variables are stored. From these joint variables values, poses are computed by means of a numerical forward kinematic model. The physical set-up implies that these poses should lie on a straight line. Hence, the straightness of the line is computed for the two kinematic parameter sets (*a priori* and identified) as the root mean square of the distance between the different positions and the line estimated by a least squares criterion. The experiment is conducted with two different orientations of the ruler. The results are presented in Table 6. For Model 12, the straightness improvement is equal to 63% and 75% , which confirms the first validation. For Model 31, the improvement is actually lower, with a relative gain around 50% for the two experiments. The low decrease of straightness improvement can be due to several factors. The first one is the diminution of the ratio between the pose number and the kinematic parameter number, even if this ratio remains acceptable (36 parameters and 284 equations). The second factor is the identifiability problem bound to the use of an exteroceptive measuring device. Eventually the hypothesis concerning the spatial parallelograms may be questionable, and a kinematic model taking into account the geometry of the rods may be necessary.

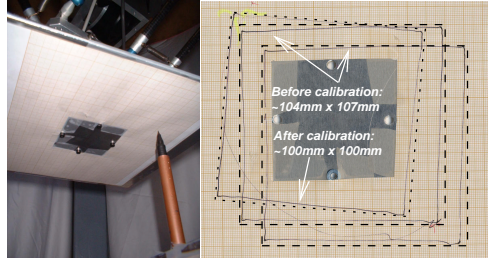


Figure 14: Validating the model by control: set-up (left) and result (right).

With the control law Another validation is performed by introducing the identified kinematic parameters in the control law, which uses Model 12. The end-effector is then displaced along a $100\text{mm} \times 100\text{mm}$ square trajectory, visualized graphically (Figure 14). The error committed on the square side is reduced from 5mm to less than 0.5mm .

6 Conclusions

In this article, the kinematic calibration of a H4 parallel mechanism using a vision-based measuring device was presented.

Composed of a single camera and screen-displayed calibration boards, the system is low-cost, easy to use, and the pose measurement enables one to perform calibration using the standard calibration method based on the Inverse Kinematic Model. Precision in the order of $1\mu\text{m}$ for 2 translations and 10^{-3}deg for the 3 rotations have been estimated for a displacement of 400mm . These specifications may be improved by the use of now available higher resolution CCD sensors, and by the introduction of a second camera to improve measurement performance on the third translation measurement. However, the system is still hampered by the loss of contrast when observing an LCD monitor.

Nevertheless, using the same methodology with a standard calibration board, a final positioning accuracy of the end-effector lower than 0.5mm could be obtained, and the accuracy improvement has been confirmed by several validation experiments. The vision-based measuring device allows us also to qualify directly the assumption validity concerning the number of degrees of freedom. For such a mechanism with less than six degrees of freedom, the parameter identifiability has been analyzed, showing that all the parameters related to the sensor installation cannot be identified.

The lower results with the second presented kinematic model need further analysis concerning the modelling of the spatial parallelograms. To get more information about the kinematics of the mechanism, the use of the camera to look at the legs of the mechanism will be also further investigated.

Acknowledgements

This study was jointly funded by CPER Auvergne 2001-2003 program and by the CNRS-ROBEA program through the MAX project. During this work, Pierre Renaud was conducting his Ph.D. at LaRAMA and LASMEA.

References

- [AHE01] N. Andreff, R. Horaud, and B. Espiau. Robot hand-eye calibration using structure-from-motion. *Int. J. Robotics Research*, 20(3):228–248, 2001.
- [CSP99] J.F. Curtino, D.E. Schinstock, and M.J. Prather. Three-dimensional metrology frame for precision applications. *Precision Engineering*, 23:103–112, 1999.
- [Dan99] D. Daney. Self calibration of Gough platform using leg mobility constraints. In *Proc of the 10th world congress on the theory of machine and mechanisms*, pages 104–109, 1999.
- [Dan00] D. Daney. *Etalonnage géométrique des robots parallèles*. PhD thesis, Université de Nice - Sophia Antipolis, 2000.
- [DRLR89] M. Dhome, M. Richetin, J.T. Lapreste, and G. Rives. Determination of the attitude of 3-D objects from a single perspective view. *IEEE Trans. on Pattern Analysis and Machine Intelligence*, 11(12):1265–1278, 1989.
- [FDAF96] G. Fried, K. Djouani, Y. Amirat, and C. François. A 3-d sensor for parallel robot calibration. a parameter perturbation analysis. In *Recent Advances in Robot Kinematics*, pages 451–460, 1996.
- [GH94a] Z. Geng and L.S. Haynes. An effective kinematics calibration method for Stewart platform. In *Proc. of Fifth International Symposium on Robotics and Manufacturing*, pages 87–92, Hawaiï, 1994.
- [GH94b] Z.J. Geng and L.S. Haynes. A "3-2-1" kinematic configuration of a Stewart platform and its application to six degrees of freedom pose measurements. *Robotics and Computer-Integrated Manufacturing*, 11(1):23–34, 1994.
- [HM93] R. Horaud and O. Monga. *Vision Par Ordinateur - Outils Fondamentaux*. Hermès, Paris, 1993. ISBN 2-86601-370-0.
- [ISO94] ISO. Iso 5725-1:1994 : Accuracy (trueness and precision) of measurement methods and results - part 1: General principles and definitions, 1994.

- [KB99] W. Khalil and S. Besnard. Self calibration of Stewart-Gough parallel robots without extra sensors. *IEEE Trans. on Robotics and Automation*, pages 1758–1763, 1999.
- [KD99] W. Khalil and E. Dombre. *Modélisation, Identification et Commande des Robots*. Hermès, 1999.
- [LVD98] JM. Lavest, M. Viala, and M. Dhome. Do we really need an accurate calibration pattern to achieve a reliable camera calibration. In *Proceedings of ECCV98*, pages 158–174, Freiburg, June 1998.
- [MCKP02] F. Marquet, O. Company, S. Krut, and F. Pierrot. Enhancing parallel robots accuracy with redundant sensors. In *Proc. of ICRA02*, pages 4114–4119, Washington, May 2002.
- [Mer97] J.P. Merlet. *Les Robots Parallèles*. Hermès, Paris, 1997.
- [MJ95] O. Masory and Y. Jiahua. Measurement of pose repeatability of Stewart platform. *J. of Robotic Systems*, 12(12):821–832, 1995.
- [PMCG01] F. Pierrot, F. Marquet, O. Company, and T. Gil. H4 parallel robot : Modeling, design and preliminary experiments. In *Proc. of ICRA01*, pages 3256–3261, Seoul, Korea, 2001.
- [RADM02] P. Renaud, N. Andreff, M. Dhome, and P. Martinet. Experimental evaluation of a vision-based measuring device for parallel machine-tool calibration. In *Proc. of IROS02*, pages 1868–1873, Lausanne, October 2002.
- [Ren03] Pierre Renaud. *Apport de la vision pour l'identification géométrique de mécanismes parallèles*. PhD thesis, Université Blaise Pascal, Clermont-Ferrand, France, September 2003.
- [Ric98] J. Richalet. *Pratique de L'identification*. Hermès, 1998.
- [Sch93] K. Schroer. *Robot Calibration*, chapter Theory of kinematic modelling and numerical procedures for robot calibration, pages 157–196. Chapman & Hall, 1993.
- [SZ99] T. Schmitz and J. Zlegert. A new sensor for the micrometre-level measurement of three-dimensional, dynamic contours. *Measurement Science Technology*, 10:51–62, 1999.
- [TL89] R.Y. Tsai and R.K. Lenz. A new technique for fully autonomous and efficient 3D robotics hand/eye calibration. *IEEE Trans. on Robotics and Automation*, 5(3):345–358, 1989.

- [TTM95] L. Tancredi, M. Teillaud, and J.-P. Merlet. Forward kinematics of a parallel manipulator with additional rotary sensors measuring the position of platform joints. In J.-P. Merlet and B. Ravani, editors, *Computational Kinematics*, pages 261–270, Dordrecht, 1995.
- [VC98] P. Vischer and R. Clavel. Kinematic calibration of the parallel delta robot. *Robotica*, 16:207–218, 1998.
- [VPG94] M. Vincze, J.P. Prenninger, and H. Gander. A laser tracking system to measure position and orientation of robot end-effectors under motion. *Int. J. Robotics Research*, 13(4):305–314, 1994.
- [WA92] C. Wampler and T. Arai. Calibration of robots having kinematic closed loops using non-linear least-squares estimation. In *IFTToMM*, pages 153–158, Nagoya, September 1992.
- [WM93] J. Wang and O. Masory. On the accuracy of a Stewart platform - Part I : The effect of manufacturing tolerances. In *Proc. of ICRA93*, pages 114–120, 1993.
- [Zhu97] H. Zhuang. Self-calibration of parallel mechanisms with a case study on Stewart platforms. *IEEE Trans. on Robotics and Automation*, 13(3):387–397, 1997.
- [ZR93] H. Zhuang and Z.S. Roth. Method for kinematic calibration of Stewart platforms. *J. of Robotic Systems*, 10(3):391–405, 1993.
- [ZYM98] H. Zhuang, J. Yan, and O. Masory. Calibration of Stewart platforms and other parallel manipulators by minimizing inverse kinematic residuals. *J. of Robotic Systems*, 15(7):395–405, 1998.